Inorganic Chemistry
Article
pubs.acs.org/IC

Alkali-Metal-Ion-Directed Self-Assembly of Redox-Active Manganese(III) Supramolecular Boxes

Gustavo González-Riopedre,[†] Manuel R. Bermejo,[‡] M. Isabel Fernández-García,*[,†] Ana M. González-Noya,[†,‡] Rosa Pedrido,[†,‡] M. Jesús Rodríguez-Doutón,[†,§] and Marcelino Maneiro*[,†]

[†]Departamento de Química Inorgánica, Facultade de Ciencias, Universidade de Santiago de Compostela, 27002 Lugo, Spain

[‡]Centro de Investigación en Química Biolóxica e Materiais Moleculares, Universidade de Santiago de Compostela, 15782 Santiago de Compostela, Spain

S *Supporting Information*

ABSTRACT: The ability to organize functional molecules into higher dimensional arrays with well-defined spatial relationships between the components is one of the major goals in supramolecular chemistry. We report here a new route for the preparation of supramolecular boxes, incorporating two types of metal ions: (i) alkali-metal ions, which induce the supramolecular architecture and essentially play a structural role in the final compounds; (ii) manganese(III) ions, which are redox-active systems and give functionality to the new cages. Our results evidence that the size of the cavity inside the box can be tuned depending on the alkali metal used, a characteristic that gives this new family of compounds the potential to act selectively against different substrates. These compounds behave as active catalysts for disproportionation of H_2O_2 or for water photolysis, but they catalyze neither catecholase reaction nor peroxidase action upon using bulky organic substrates.

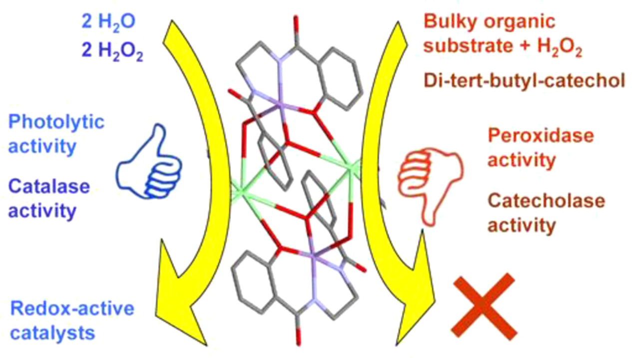

■ INTRODUCTION

Metal–organic solids containing cavities or channels with controlled sizes, shapes, and chemical environments have become increasingly important because some of these supramolecular structures may have functional properties and specific applications in various fields, including host–guest chemistry, redox activity, magnetic behavior, photo- and electrochemical sensing, and catalysis.[1−5]

Metal-directed self-assembly[6] constitutes one of the outstanding strategies to obtaining supramolecular architectures; a particular advantage of this method is the single-step assembly process involving simple mixing of metals and ligands rather than a stepwise approach.[7]

The typical metal-assisted process involves the use of a transition-metal ion to induce the assembly of the structure, but the use of alkali-metal cations is relatively rare because it is more difficult to control the architecture because of the variety of coordination numbers and weak coordination ability of such ions in comparison to transition-metal ions (Chart 1).[8,9]

The electronic component of ligand binding to alkali-metal ions can generally be considered in terms of simple electrostatics. In fact, these cations may be characterized as a sphere of positive charge that generally attracts donors with little regard for ligand orientation.[10]

Chart 1. Schematic Representation of Our Synthetic Approach to the Assembly of Manganese(III) Boxes with Alkali-Metal Ions[a]

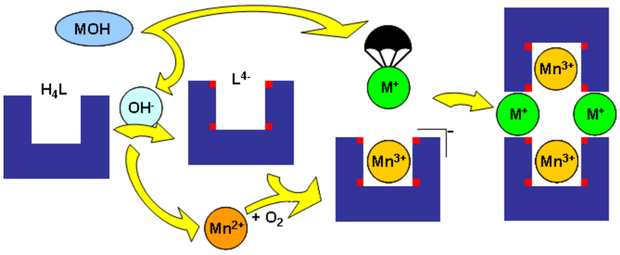

[a]The red dots in the ligand represent the negative charges after deprotonation of the phenoxo and amide groups. The alkali-metal cation makes stabilization of this novel supramolecular motif possible.

In contrast to simple salt association and because of the lack of selectivity and the long-range character of the Coulombic interactions, ionic self-assembly must also involve distinct geometrical shapes, functionality patterns, and distributions of cohesion energy along the charged objects; i.e., it is "real" supramolecular chemistry in which the secondary structural elements support the alignment in a process driven by the charge–charge coupling.[11−13]

We have previously studied ionic self-assembly processes to obtain functional manganese(III)–Schiff base networks using

Received: August 2, 2014
Published: February 23, 2015

DOI: 10.1021/ic501842x

different counteranions such as perchlorate, nitrate, chloride, carboxylates, etc.[14] The results of these studies show that the nature of the anion can control the architecture in the final products from the self-assembly process.

In the work described here, we further explored these simple and versatile methods in order to establish the first strategy to connect redox-active manganese(III) complexes through spherical alkali-metal cations. The self-assembly of manganese compounds directed by alkali-metal ions could generate novel supramolecular motifs that improve the important properties of manganese(III) complexes.

The challenge of controlling the combination of transition- and alkali-metal ions in an assembled supramolecular structure was overcome by using the appropriate ligand. For this purpose, we selected the tetraionic H_4L bisamido−bisphenoxy ligand (Chart 2), which contains six potential donor atoms: two amide nitrogen (N_a), two phenoxo (O_p), and two amide oxygen (O_a) atoms. The $2N_a2O_p$ core forms an inner cavity that is able to accommodate one metal ion. The amido donor groups have the potential to stabilize higher oxidation states of manganese,[15] and, in addition, the configuration of the two amide oxygen atoms, which point toward the outside of the inner cavity, facilitates an extension of the dimensionality of the structure.

Chart 2. Ligand H_4L

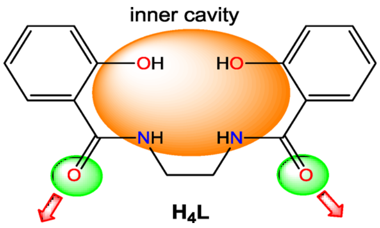

EXPERIMENTAL METHODS

Chemical and Reagents. All of the starting materials (Aldrich) and solvents (Probus) used for the synthesis were of commercially available reagent grade and were used without further purification.

Physical Measurements. Elemental analyses were performed on a Carlo Erba model 1108 CHNS-O elemental analyzer. IR spectra were recorded as KBr pellets on a Bio-Rad FTS 135 spectrophotometer in the range of 4000−400 cm^{-1}. ^1H NMR spectra were recorded on a Bruker AC-300 spectrometer using CD_3OD (296 K) as the solvent and $SiMe_4$ as an internal reference. Electrospray ionization mass spectrometry (ESI-MS) spectra of the compounds were obtained on a Hewlett-Packard model LC-MSD 1100 instrument (positive-ion mode, 98:2 $CH_3OH/HCOOH$ as the mobile phase, 30−100 V). Room-temperature magnetic susceptibilities were measured using a MSB-MKI digital measurement system, calibrated using mercury tetrakis(isothiocyanato)cobaltate(II) ($Hg[Co(NCS)_4]$) as the susceptibility standard. Variable-temperature magnetic data for **3** were obtained with a Quantum Design MPMS SQUID susceptometer. The sample was a 3-mm-diameter pellet molded from a ground crystalline sample. Magnetic data for **1** and **2** were obtained with a Quantum Design PPMS susceptometer. Electronic spectra were recorded on a Cary 230 spectrometer. The conductivities of 10^{-3} M solutions in *N,N*-dimethylformamide (DMF) were measured on a Crison micro CM 2200 conductivimeter.

Synthesis of the H_4L ligand. The ligand H_4L was prepared by the reaction of phenyl salicylate and 1,2-ethylendiamine in a 2:1 molar ratio at 180−190 °C for 1 h. The product was treated with diethyl ether to obtain a white powder at almost quantitative yield. Mp: 180 °C. Anal. Calcd for $C_{16}H_{16}N_2O_4$ (300.3): C, 64.0; H, 5.4; N, 9.3. Found: C, 64.0; H, 5.5; N, 9.4. ESI-MS: *m/z* 301 ($\{H_4L + H\}^+$). IR (KBr, cm^{-1}): ν(N−H) 3408 (vs), ν(O−H) 3063 (m), ν(amide I, C=O) 1646 (m), ν(amide II, C−N, N−H) 1550 (m), ν(C−O) 1253 (s). ^1H NMR (DMSO-d_6): δ 2.48 (s, 4H), 6.85 (t, 4H), 7.36 (t, 2H), 7.80 (d, 2H), 8.95 (s, 2H). ^{13}C NMR (DMSO-d_6): δ 39.4 ($-CH_2-$), 55.7 ($=NCH_2-$), 57.0 ($-OCH_3$), 116.4−134.2 (C_{ar}), 161.1 (C−OH), 169.9 (C=O).

Synthesis of the Complexes. All of the manganese(III) complexes were prepared by stirring a methanol (MeOH) solution (50 mL) of the corresponding ligand and subsequently adding a MeOH solution of metal hydroxide (30 mL) and a MeOH solution of $Mn(Ac)_2{\cdot}4H_2O$ at room temperature. The initial light color of the solutions rapidly changed to red-brown. After 3 h of stirring at room temperature, slow evaporation of the solvent led to the deposition of brown compounds. The products were collected by filtration, washed with diethyl ether (2 × 20 mL), and then dried in vacuo.

$[KMnL(CH_3OH)]_2{\cdot}CH_3OH{\cdot}H_2O$ (1). H_4L (0.3 g, 1.00 mmol), $Mn(Ac)_2{\cdot}4H_2O$ (0.25 g, 1.00 mmol), and K(OH) (0.06 g, 1.00 mmol) were reacted. Yield: 0.32 g (71%). Selected data for **1** are as follows. ESI-MS: *m/z* 353 ($\{MnL + 2H\}^+$), 393 ($\{KMnL + H\}^+$), 782 ($\{[KMnL]_2 + H\}^+$). Elem anal. Calcd for $C_{35}H_{38}K_2Mn_2N_4O_{12}$: C, 46.8; H, 4.1; N, 6.1. found: C, 46.5; H, 4.0; N, 6.1. IR (cm^{-1}): ν(O−H) 3386 (m), ν(amide I, C=O) 1599 (m), ν(amide II, C−N, N−H) 1530 (m), ν(C−O) 1256 (s). Magnetic moment: μ_{eff} = 4.8 μ_B. ^1H NMR paramagnetic (DMSO-d_6): δ −22.80 (H4), −19.50 (H5). λ (ε) = 510 nm (700 M^{-1} cm^{-1}).

$[Rb_2Mn_2L_2(CH_3OH)(H_2O)]{\cdot}3H_2O$ (2). H_4L (0.3 g, 1.00 mmol), $Mn(Ac)_2{\cdot}4H_2O$ (0.25 g, 1.00 mmol), and Rb(OH) (0.10 g, 1.00 mmol) were reacted. Yield: 0.47 g (48%). Selected data for **2**are as follows. ESI-MS: *m/z* 353 ($\{MnL + 2H\}^+$), 438 ($\{RbMnL + H\}^+$), 876 ($\{[RbMnL]_2 + H\}^+$). Elem anal. Calcd for $C_{33}H_{36}Mn_2N_4O_{13}Rb_2$: C, 40.5; H, 3.7; N, 5.7. Found: C, 41.1; H, 3.5; N, 5.9. IR (cm^{-1}): ν(C−O, amide I) 1599, ν(amide II) 1526, ν(C−O) 1261, ν(O−H) 3421. Magnetic moment: μ_{eff} = 4.9 μ_B. ^1H NMR paramagnetic Mn^{III} (DMSO-d_6): δ −24.2, −16.3. λ (ε) = 512 nm (420 M^{-1} cm^{-1}).

$[CsMnL(H_2O)]_2$ (3). H_4L (0.3 g, 1.00 mmol), $Mn(Ac)_2{\cdot}4H_2O$ (0.25 g, 1.00 mmol), and Cs(OH) (0.15 g, 1.00 mmol) were reacted. Yield: 0.29 g (68%). Selected data for **3** are as follows. ESI-MS: *m/z* 353 ($\{MnL + 2H\}^+$), 485 ($\{CsMnL + H\}^+$), 970 ($\{[CsMnL]_2 + H\}^+$). Elem anal. Calcd for $C_{32}Cs_2H_{28}Mn_2O_{10}$: C, 38.3; H, 2.8 N, 5.6. Found: C, 38.2; H, 2.6; N, 5.5. IR (cm^{-1}): ν(O−H) 3408 (m), ν(amide I, C=O) 1598 (m), ν(amide II, C−N, N−H) 1531 (m), ν(C−O) 1258 (s). Magnetic moment: μ_{eff} = 4.6 μ_B. ^1H NMR paramagnetic Mn^{III} (DMSO-d_6): δ −22.28 (H4), −19.82 (H5). λ (ε) = 514 nm (380 M^{-1} cm^{-1}).

Crystallography. Single crystals of the ligand H_4L and of the complexes **1**−**3** suitable for X-ray diffraction studies were obtained by slow evaporation of the methanolic solution at room temperature. Detailed crystal data collection and refinement are summarized in Tables 1 and 2. Intensity data were collected on a Bruker Smart CCD-1000 diffractometer employing graphite-monochromated Mo Kα radiation (λ = 1.54184 Å) for **1** and **3** at 120 K, for **2** at 110 K, and for H_4L at 100 K. The structures were solved by direct methods[16] and finally refined by full-matrix least squares based on F^2. An empirical absorption correction was applied using *SADABS*.[17] All non-hydrogen atoms were included in the model at geometrically calculated positions. Drawings of the molecules were generated with the *ORTEP-3*[18] and *Mercury 3.1* programs.[19]

Studies on the Catalase-like Function. A 10 mL flask containing a solution of the complexes in MeOH (3 mL, 1 mM) was sealed with a septum and connected to a gas-measuring buret (precision of 0.1 mL) through a double-ended needle. The solution was stirred at constant temperature on a water (H_2O) bath. Catalysis was initiated by introducing a hydrogen peroxide (H_2O_2) solution (1 mL, 2.5 M) using a syringe, and the evolved dioxygen (O_2) was volumetrically measured.

Photolysis Experiments. Irradiation of aqueous solutions of the complexes was carried out in a colorless two-necked glass flask (1 L) placed in a methacrylate thermostated H_2O bath. A magnetically stirred solution of the corresponding complex (5 × 10^{-6} mol) and *p*-

DOI: 10.1021/ic501842x
Inorg. Chem. 2015, 54, 2512−2521

Table 1. Crystal Data and Structure Refinement for H_4L and 1

	H_4L	1
empirical formula	$C_{16}H_{16}N_2O_4$	$C_{35}H_{36}K_2Mn_2N_4O_{12}$
fw	300.31	892.76
temperature/K	100	110
wavelength/Å	0.71073	0.71073
cryst syst	triclinic	triclinic
space group	$P\bar{1}$	$P\bar{1}$
a/Å	6.545(3)	9.570(6)
b/Å	6.964(3)	10.427(6)
c/Å	15.297(8)	10.825(6)
α/deg	94.318(8)	113.065(7)
β/deg	94.205(10)	97.273(8)
γ/deg	95.464(16)	100.410(8)
V/Å^3	689.9(6)	954.0 (10)
Z	2	2
D/mg m^{-3}	1.446	1.554
μ/mm^{-1}	0.105	0.947
F(000)	316	458.0
θ range/deg	1.34−25.68	2.10−23.82
reflns collected	2589	5100
indep reflns	2589	2932
data/restraints/param	2589/0/247	2932/2/266
GOF	0.884	0.966
R1, wR2 [$I > 2\sigma(I)$]	0.0708, 0.1799	0.0706, 0.1720
R1, wR2 (all data)	0.1256, 0.2117	0.1307, 0.2036

Table 2. Crystal Data and Structure Refinement for 2 and 3

	2	3
empirical formula	$C_{33}H_3Rb_2Mn_2N_4O_{13}$	$C_{16}H_{14}CsMnN_2O_5$
fw	977.48	502.14
temperature/K	120	110
wavelength/Å	0.71073	0.71073
cryst syst	monoclinic	monoclinic
space group	$P2_1$	$P2_1/c$
a/Å	9.6398(15)	10.839(2)
b/Å	17.688(3)	15.437(3)
c/Å	10.5316(17)	9.3724(19)
α/deg	90	90
β/deg	102.232(3)	92.052(4)
γ/deg	90	90
V/Å^3	1754(5)	1567.2(5)
Z	2	4
D/mg m^{-3}	1.850	2.128
μ/mm^{-1}	3.549	3.163
F(000)	980	976
θ range/deg	1.98−27.48	1.88−27.88
reflns collected	7897	28977
indep reflns	7897	3736
data/restraints/param	7897/6/503	3736/0/232
GOF	1.095	1.098
R1, wR2 [$I > 2\sigma(I)$]	0.0329, 0.0695	0.0374, 0.0699
R1, wR2 (all data)	0.0443, 0.075	0.0618, 0.0749

benzoquinone (BQ; 2×10^{-4} mol, 21 mg) in deoxygenated and deionized H_2O was irradiated with light (in the 350−2500 nm range) from a 200 W tungsten lamp for 24 h. The solution was connected to a UV spectrophotometer through a peristaltic pump and a flow cell. Quantitative measurements of O_2 formed during irradiation were performed using a dissolved-oxygen probe-type electrode (Crison Oxi45P). In a typical experiment, deionized and deoxygenated H_2O was placed in a two-necked glass flask: one neck contained the oxygen electrode and the second a septum. The whole flask arrangement was immersed in a thermostated bath so that H_2O came up to the base of the necks. Stirring was begun, the complex and quinone were added, and the septum was fitted to make the system airtight. Four needles were pushed through the septum, one reaching into the liquid, and a stream of argon was introduced into the solution until the reading of the oxygen meter fell to <3%. Once this value was reached, the argon and purge needles were removed, and the system was left stirring for 10 min to equilibrate. The light was switched on. Only the two needles connected to the flow cell remained through the septum. Oxygen readings were recorded as a percentage of dissolved oxygen, where 100% corresponds to a fully saturated aqueous solution at 25 °C (6 cm^3 O_2 dm^{-3}) and 0% corresponds to no dissolved oxygen. Reproducible results were obtained with this method provided that the temperature of the bath remained constant (25.0 ± 0.1 °C) and a constant stirring rate was maintained.

Peroxidase Probes. Oxidation of 2,2′-azinobis(3-ethylbenzothiazoline)-6-sulfonic acid (ABTS) with H_2O_2 at ca. pH 7 in the presence of the complexes was tested in the following manner. An aqueous solution of ABTS (50 μL, 0.009 M, 4.5×10^{-7} mol) and a methanolic solution of the complex (10 μL, 10^{-3} M, 10^{-8} mol) were added to H_2O (3 mL). The intensity of the UV absorption bands of ABTS started to increase immediately after the addition of an aqueous solution of H_2O_2 (50 μL, 10 M, 5×10^{-4} mol). Spectra were recorded every 30 s, and the data reported in Table 5 correspond to the maximum observed values.

Oxidation of 3,4-Dimethoxybenzyl Alcohol (Veratryl Alcohol, VA). VA (200 mmol, 0.29 mL), previously dissolved in 20 mL of a dihydrogen phosphate/NaOH buffer at pH 8, was mixed with a methanolic solution (15 mL) of the catalytic complex (0.5 mmol, ca. 6 mg). The oxidant (600 mmol) was added in three portions at 20 min intervals. The reaction mixture was stirred for 10 h at 22 °C with an air flow bubbling through the solution and then filtered through a short silica gel plug to remove the catalyst and excess oxidant. The reaction mixture was extracted in CH_2Cl_2 in the presence of a saturated aqueous NaCl solution. The organic layer was dried over $MgSO_4$ and evaporated under reduced pressure. The mixture was then purified by column chromatography using a 1:1 mixture of ethyl acetate/hexane as the eluent.

Guaiacol Oxidation Assay. Measurements of the oxidation activities were performed at 20 °C in H_2O. A mixture of the complex (10^{-4} M, 29.1 μL, MeOH) and guaiacol (0.1 M, 10 μL, MeOH) in a total volume of 3.0 mL was used, and then 60 μL of 1 M H_2O_2 (in H_2O) was added. The initial rate of guaiacol oxidation was determined from an increase in the absorbance at 470 nm (ε_{470} = 26600 M^{-1} cm^{-1}).

Catecholase Activity. With 3,5-di-*tert*-butylcatechol (3,5-$DTBCH_2$) as the substrate, catecholase activity is studied by monitoring UV−vis spectra because the oxidized product, 3,5-di-*tert*-butylquinone (3,5-DTBQ), has a characteristic band at ca. 400 nm. To check the ability of the complexes to behave as catalysts for catecholase activity, a 10^{-5} M solution of the complex was treated with a 100-fold concentrated solution of 3,5-$DTBCH_2$, and the spectra were recorded up to 60 min. Experiments were done in both DMF and MeOH. It may be noted here that a blank experiment without a catalyst does not show formation of the quinone up to 8 h in DMF and 6 h in MeOH.

■ RESULTS AND DISCUSSION

The synthesis of the new manganese(III) alkali-metal ion supramolecular boxes is achieved by the treatment of a methanolic solution of the bisamido−bisphenoxy ligand H_4L with an alkali-metal hydroxide and a manganese(II) salt, as detailed in the Experimental Methods section. The alkali-metal hydroxide plays multiple roles in this new approach. It provides the basic conditions required to achieve tetradeprotonation of the ligand and oxidation of manganese(II) to manganese(III) in the presence of oxygen, with these being the expected roles already known in classical manganese(III) chemistry. In our route, the alkali-metal cation also has two additional functions: it counteracts the negative charge of the $[MnLD]^-$ tectons, and it also has a structural role, both of which are crucial for the assembly of the final supramolecular boxes (see Chart 1).

Elemental analysis establishes their formulas as $[KMnL(CH_3OH)]_2 \cdot CH_3OH \cdot H_2O$ (**1**), $[Rb_2Mn_2L_2(CH_3OH)(H_2O)] \cdot 3H_2O$ (**2**), and $[CsMnL(H_2O)]_2$ (**3**), which are consistent with the formation of the neutral dimeric species of the formula $[M^IMn^{III}L(D)]_2$, where L is the tetradeprotonated ligand, D represents H_2O or MeOH, and M is the alkali-metal ion (K for **1**, Rb for **2**, and Cs for **3**). These formulations are in agreement with molar conductivity measurements in 10^{-3} M DMF solutions, which are at about 20−30 μS cm^{-1}, typical of nonelectrolyte complexes.[20] Furthermore, other spectroscopic techniques support such formulas and give insight into both the solid and solution structure of the complexes.

All of the complexes share some similar features in the IR spectra (Figure S7 in the Supporting Information, SI), exhibiting a strong band between 1605 and 1598 cm^{-1} characteristic of the ν(amide I, C=O) stretching mode, which is shifted 45−38 cm^{-1} lower with respect to the free ligand, and a band 1565−1522 cm^{-1} of the ν(amide II) stretching mode, which is shifted 13−8 cm^{-1} lower with respect to the free ligand (Figure S3 in the SI). The band attributed to the ν(C−O) mode is also shifted 7−11 cm^{-1} to higher frequencies with respect to the free ligand. These data suggest coordination of the ligand through the inner phenol oxygen and the amide nitrogen atoms. Strong bands centered at ca. 3400 cm^{-1} can be assigned to a combination of the ν(O−H) modes of coordinated and lattice H_2O/MeOH, now present in the complexes.

ESI-MS spectra registered in MeOH show peaks corresponding to the fragment $[MnL]^+$ for all of the complexes, indicating coordination of the manganese ion to the deprotonated ligand. Other signals could be assigned to $[MMnL]^+$ and $[M_2Mn_2L_2]^+$ units, which could be attributed to the presence of dimeric species (Figure S6 in the SI).

The electronic spectroscopic data recorded are very similar for all compounds **1**−**3**, indicating that the manganese(III) complexes are behaving as high-spin octahedral d^4 systems, probably suffering a significant Jahn−Teller distortion, which affects the spectra and complicates its interpretation. A broad shoulder at about 509−520 nm (ε = 380−700 M^{-1} cm^{-1}) is attributable to a d−d transition, while it is reasonable to assign the broad band obtained at 480−490 nm (ε = 2600−3300 M^{-1} cm^{-1}) to the phenolate → manganese(III) charge transfer. The energy and intensity of the ligand-to-metal charge-transfer and d−d transitions are in agreement with those reported for related manganese(III) complexes.[21,22]

Paramagnetic ^1H NMR studies of the complexes were registered using DMSO-d_6 as the solvent, and the data serve to substantiate the formation of manganese(III) complexes. The data interpretation was based on previous findings for manganese(III) complexes made by Pecoraro and co-workers[23] and in our own results.[24] The data are collected in the Experimental Methods section, and Figure S8 in the SI shows one of these spectra. The spectra contain two upfield proton resonances, outside the diamagnetic region (δ 0−14), due to the isotropic shifting of the ligand protons for high-spin manganese(III) complexes in an octahedral field. The signals must arise from the H4 and H5 protons of the aromatic phenoxy rings. The signals between δ −20.73 and −30.52 arise from the H4 protons, while the resonances from δ −15.70 to −21.50 arise from the H5 protons. Our experience shows that signals in ortho positions to donor atoms are not observable for these kinds of complexes by paramagnetic ^1H NMR spectroscopy.

Crystallographic Studies. The main crystallographic data for H_4L are summarized in Table 1, and bond lengths and angles are listed in Table S1 in the SI.

The crystal structure of H_4L reveals that it exists as discrete molecules (Figure 1). The C8−N10 and N13−C14 distances of 1.342(4) and 1.340(4) Å, respectively, are practically identical and consistent with C−N single bonding. The two oxygen atoms O1 and O22 are forming phenolic groups, and the observed O1−C2 and C21−O22 bond distances of 1.360(4) and 1.351(4) Å, respectively, are consistent with the C−O single bonds.

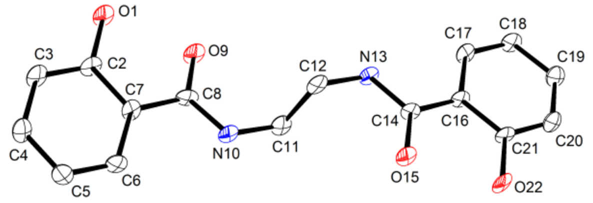

Figure 1. Molecular structure of H_4L showing the atomic numbering scheme. The hydrogen atoms are omitted.

The external C−O amide bond distances, C14−O15 1.257(2) Å and C8−O9 1.260(3) Å, are smaller than the C−O phenolic distance and consistent with the C−O double bonds.[25] Intramolecular hydrogen bonds exist between the hydrogen atoms H1 and H22 of phenolic oxygen atoms O1 and O22 and the neighboring amidic oxygen atoms O9 and O15, respectively: [H1···O9 1.57(4) Å, O1−H1···O9 2.502(3) Å; O1−H1···O9 156(3)°] and [H22···O15 1.67 (4) Å, O22−H22···O15 2.504(3) Å; O22−H22···O15 152(3)°] (Figure S5 in the SI).

One of the two aromatic rings is arranged almost perpendicular to the tetradentate cavity O22−N13−N10−O9. The conformation of the free ligands in the solid state is of particular interest in relation to that required in a metal complex. This ligand, with a flexible spacer, produces these types of open structures, as we have previously found in similar ligands.[26] Clearly, this conformation is not suitable for direct coordination to a metal ion in the usual arrangement for a tetradentate ligand. Therefore, significant rearrangement of the molecule must occur, involving rotation about the C11−C12 bond to give a near-eclipsed conformation, for possible mononuclear complexation. The amide nitrogen atom is a strong field ligand favoring N-coordination of the planar tetradentate ligand, although rare examples of coordination via the oxygen atom of the deprotonated amide group and deviation from planarity have been encountered.[27]

Slow evaporation of the mother liquors allowed us to obtain brown crystals of **1**−**3**, from which the molecular structure was determined by X-ray crystallography. The main crystal data and structure refinement details are collected in Tables 1 and 2. The crystal structures of the compounds reveal the existence of dimeric supramolecular boxes. Selected bond lengths and angles for these structures are collected in Tables 3 and 4.

Different drawings showing the crystal structure of these supramolecular boxes are shown in Figures 2−4. Figure 2

Table 3. Important Bond Lengths (Å) of Compounds 1–3[a]

	1	2A	2B	3
Mn–O_p	1.870(4)	1.874(3)	1.863(3)	1.863(3)
	1.878(5)	1.894(3)	1.883(3)	1.889(3)
Mn–N_a	1.927(6)	1.939(3)	1.925(3)	1.951(3)
	1.933(6)	1.960(3)	1.942(3)	1.955(3)
Mn–O_{ax}	Mn–O5 2.230(6)	Mn2A–O26w 2.175(3)	Mn2B–O27 2.212(3)	Mn–O111 2.164(3)
Mn···Mn	6.514	6.667		6.746
M···M	4.472	4.731		4.870
Mn···M	3.788, 4.177	Mn2A–Rb1A 3.889, Mn2A–Rb1B 4.2735	Mn2B–Rb1B 3.836, Mn2B–Rb1A 4.344	4.1417
M–O	K–O 2.690–3.200	Rb1A–O 2.873–3.552	Rb1B–O 2.864–3.431	Cs–O 3.107–3.460

[a] O_p = $O_{phenolic}$; N_a = N_{amidic}; O_{ax} = O_{axial}; the axial oxygen atom is methanolic for **1** (O5) and **2B** (O27); the axial oxygen atom is from H_2O for **3** (O111) and **2A** (O26w).

Table 4. Important Bond Angles (deg) of Compounds 1–3[a]

Compound **1**			
O30–Mn1–O10	90.5(2)	O30–Mn1–O41	92.7(2)
O30–Mn1–N39	92.4(2)	O10–Mn1–O41	90.6(2)
O10–Mn1–N39	171.1(3)	N39–Mn1–O41	97.7(2)
O30–Mn1–N19	170.8(2)	N19–Mn1–O41	96.1(2)
O10–Mn1–N19	91.9(2)	O30–Mn1–K2	45.69(15)
N39–Mn1–N19	84.0(2)	O10–Mn1–K2	47.16(14)
Compound **2A**			
O3–Mn2–O24	89.67(12)	O3–Mn2–O26	95.78(12)
O3–Mn2–N12	92.69(13)	O24–Mn2–O26	89.43(13)
O24–Mn2–N12	172.67(15)	N12–Mn2–O26	97.23(14)
O3–Mn2–N15	167.00(13)	N15–Mn2–O26	97.18(13)
O24–Mn2–N15	91.55(13)	O3–Mn2–Rb1	46.35(9)
N12–Mn2–N15	84.61(14)	O24–Mn2–Rb1	45.42(9)
Compound **2B**			
O3–Mn2–O24	90.14(12)	O3–Mn2–O27	94.13(12)
O3–Mn2–N12	92.76(13)	O24–Mn2–O27	86.90(12)
O24–Mn2–N12	175.20(14)	N12–Mn2–O27	96.70(14)
O3–Mn2–N15	167.09(14)	N15–Mn2–O27	98.67(13
O24–Mn2–N15	92.25(13)	O3–Mn2–Rb1	46.78(9)
N12–Mn2–N15	84.09(14)	O24–Mn2–Rb1	46.41(9)
Compound **3**			
O431–Mn2–O131	89.67(12)	O431–Mn2–O111	98.59(12)
O431–Mn2–N1	166.66(14)	O131–Mn2–O111	98.59(12)
O131–Mn2–N1	90.90(13)	N1–Mn2–O111	94.69(13)
O431–Mn2–N4	92.00(13)	N4–Mn2–O111	100.72(13)
O131–Mn2–N4	165.93(14)	O431–Mn2–Cs1	44.70(8)
N1–Mn2–N4	84.30(14)	O131–Mn2–Cs1	46.26(8)

[a] O_p = $O_{phenolic}$; N_a = N_{amidic}; O_{ax} = O_{axial}.

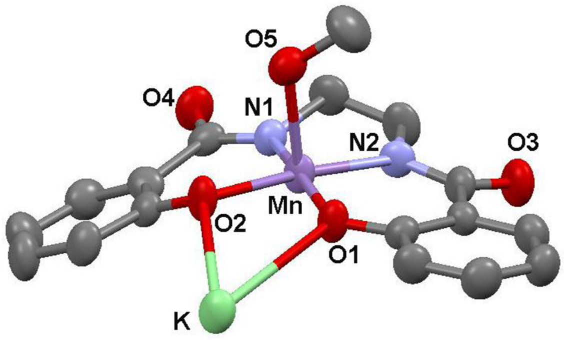

Figure 2. Coordination environment around the manganese metal center in **1**, showing the square-pyramidal geometry for this ion.

shows the coordination environment around the manganese center. In all cases, the geometry around the manganese(III) ions can be described as distorted square pyramidal. The coordination sphere around each manganese center comprises the planar bisamido ligand, which is tightly bound to the metal ion through the inner N_2O_2 compartment by the N_{amido} and O_{phenol} atoms. A fifth coordination position is completed with a solvent molecule (MeOH for **1**, H_2O for **3**; in the case of **2**, one manganese of a dimer is bonded to a H_2O molecule and the other manganese to a MeOH molecule). These $[MnLD]^-$ tectons are connected through the alkali-metal ions (M) to give the neutral dimeric $[MMnL(D)]_2$ boxes.

The structure of complex **2** (Figure 3) was found to consist of two different coordination environments for the manganese ion of the dimer because different solvent molecules (H_2O or MeOH) are bonded to the manganese ion.

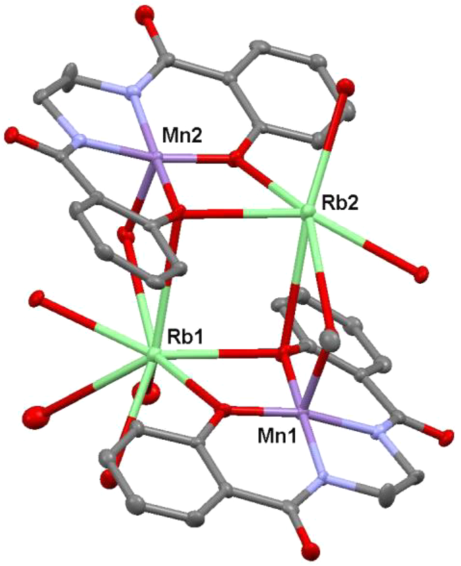

Figure 3. Molecular structure for the supramolecular box 2.

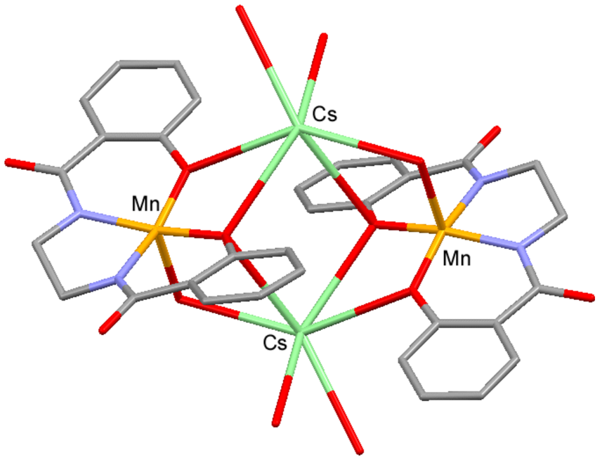

Figure 4. Stick diagram of the supramolecular box 3 (cesium cation in green, manganese ion in orange, oxygen in red, nitrogen in blue, and carbon in gray).

The cocrystallization phenomenon is rather abundant in manganese coordination chemistry,[28−30] and it points out the ability of these complexes to evolve into different structures in solution, driven by slight variations in the media. Cocrystallization usually arises when the initial and final complexes crystallize together. The supramolecular structures induced by potassium(I), rubidium(I) and cesium(I) arise from multiple M−O−Mn bridges. For instance, in the case of **3** (see Figure 4), the cesium cation is surrounded by six oxygen atoms and occupies the space between two $[\mathrm{MnLD}]^-$ tectons. This cesium(+) ion is coordinated by two phenoxo oxygen atoms (which are also bonded to a manganese ion), a phenoxo oxygen atom and a methanolic oxygen atom, both of which are bound to the second manganese ion and two amido oxygen atoms of the neighboring units. All of the Cs−O distances are in the range 3.107−3.460 Å. The relatively broad ranges of the Cs−O distances (and, in general, $\mathrm{M^I}$−O distances) are associated with increased structural flexibility and an increased capacity for close contacts between the alkali-metal ion and aromatic rings.[31] The Mn−Cs distance of 4.1417 Å is similar to those previously reported in the literature.[32] Intermolecular amido interactions connect the supramolecular boxes through cesium ions to form a 3D aggregate.

The solved crystallographic structures for **1** and **2** again show coordination of the manganese(III) ion to the inner N_2O_2 compartment of the tetraanionic L_4^- ligand. The supramolecular boxes are induced by the potassium (in **1**) or rubidium (in **2**) cation, which is able to establish a net of M−O−Mn bridges. The configuration of these boxes is depicted in Figure 5.

The size of the cavity inside the box is slightly different depending on the alkali-metal ion and increases from potassium to cesium as the size of the ion increases (see Figure 5). Thus, the distances between the manganese ions range from 6.51 Å (in **1**) to 6.75 Å (in **3**). The alkali metal−alkali metal distances also increase from 4.47 Å (in **1**) to 4.87 Å (in **3**).

Magnetic Studies. The values for the magnetic moments at room temperature for **1** and **2** are very close to the spin-only value of 4.9 μ_B, as expected for a high-spin magnetically diluted d^4 manganese(III) ion, and also in agreement with the large distances (6.5−6.7 Å) between the manganese ions shown by the molecular structures described above. The magnetic moment at room temperature for **3** is 4.6 μ_B, slightly lower than the expected value for an isolated high-spin manganese(III) ion.

Magnetic studies at variable temperature have been done for **1**−**3** (between 300 and 2 K) in a 0.8 T applied magnetic field. Antiferromagnetic behavior has been found for the three complexes.

The magnetic behavior for **3** is shown in Figure 6 as the thermal variation of the $\chi_M T$ versus T plot. χ_M is the molar magnetic susceptibility per Mn_2 unit corrected for the

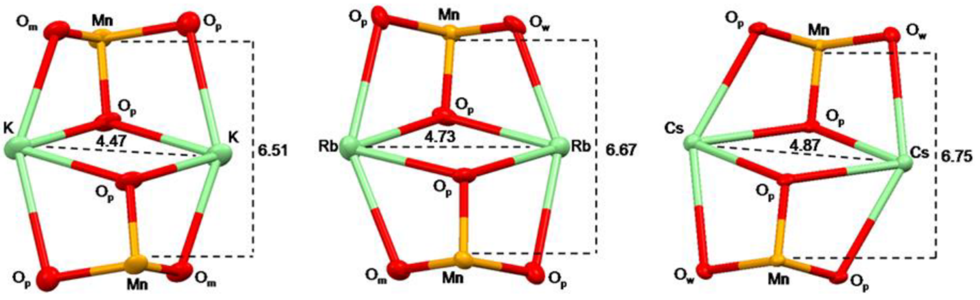

Figure 5. Supramolecular box core for **1** (left), **2** (center), and **3** (right) showing the intermetallic distances between the manganese and alkali-metal ions (values in angstroms) depicted in the middle of the dashed line connecting the pair of ions (O_p = phenolic oxygen atom; O_m = methanolic oxygen atom; O_w = water oxygen atom).

DOI: 10.1021/ic501842x
Inorg. Chem. 2015, 54, 2512−2521

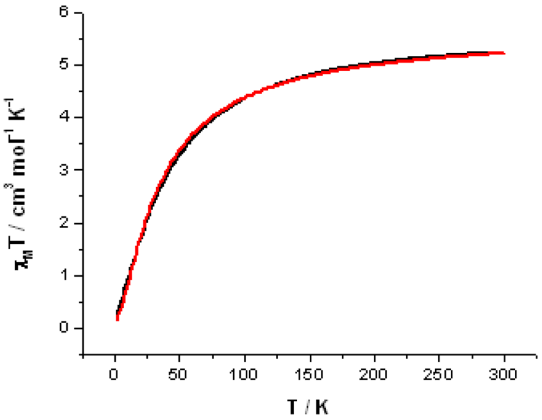

Figure 6. Temperature dependence of $\chi_M T$ on T for **3**. The black line corresponds to observed data and the red line to the best data fit, with χ_M being the molar magnetic susceptibility.

diamagnetism of the ligands.[33] It decreases smoothly from 5.22 cm^3 mol^{-1} K at 300 K to 4.37 cm^3 mol^{-1} K at 100 K. Upon further lowering of the temperature, $\chi_M T$ decreases to 0.23 cm^3 mol^{-1} K at 2 K. This behavior suggests the operation of antiferromagnetic interactions between manganese(III) ions.

According to the X-ray structure of **3**, a simple system of two exchange-coupled manganese(III) ($S = 2$) cations was considered ($H = -2JS_{\mathrm{Mn1}}S_{\mathrm{Mn2}}$) to fit these experimental data as the first step.[34] Attempts to fit the data with this simple model yielded only average results with discrepancies at lower temperatures. The introduction of a zero-field-splitting term D, common for both metal sites ($D_1 = D_2 = D$), brought about significant improvements to the fit. The estimation of the coupling constant was performed using the Hamiltonian $H = -JS_{\mathrm{Mn1}}S_{\mathrm{Mn2}} + D_{\mathrm{Mn}}[S^2_{\mathrm{Mn},z_1} + S^2_{\mathrm{Mn},z_1}]$, which includes the axial single-ion local anisotropy of the manganese(III) ions, according to the solved crystal structure.[35] This model reproduced the experimental curve very well (Figure 6), except for small disagreements at low temperature, which may be due to the simultaneous operation of intermolecular interactions between adjacent dinuclear molecules through weak contacts. These intermolecular interactions are expected to be weaker than J because of the significantly greater distances involved.[36] In fact, because the introduction of an intermolecular interaction according to the mean-field Hamiltonian $J = -2zJ\langle S_z\rangle S_z$ affords a marginal improvement to the fit of **3**, only zero-field splittings were considered in order to avoid overparametrization.

The best fit of the experimental susceptibility data with the above Hamiltonian led to the following parameters: $J = -4.6$ cm^{-1}, $D = 1.22$, the mean Landé factor $g = 1.95$, and an agreement factor R $(=\sum[(\chi T)_{\mathrm{obs}} - (\chi T)_{\mathrm{cal}}]^2/\sum(\chi_{\mathrm{obs}}T)^2)$ of 1.3×10^{-4}. Compound **3** is characterized by large Mn···Mn distances of about 6.75 Å. The small absolute value of J agrees with overlap through the 2p oxygen orbitals. The J value, showing small antiferromagnetic behavior, and the D value, are similar to those observed in other manganese(III) dimers.[37]

Attempts to fit the magnetic data for **1** and **2** with the previous model using the simple system of two exchange-coupled manganese(III) ($H = -2JS_{\mathrm{Mn1}}S_{\mathrm{Mn2}}$) or the Hamiltonian with the axial single-ion local anisotropy of the manganese(III) ions ($H = -JS_{\mathrm{Mn1}}S_{\mathrm{Mn2}} + D_{\mathrm{Mn}}(S_{\mathrm{Mn},z_1}{}^2 + S_{\mathrm{Mn},z_1}{}^2)$ were unsuccessful to simulate the experimental results. The best fit to the experimental data (Figure 7) was obtained with the latter model with a formula that includes some impurity (f) arising from manganese(III) monomeric species. A satisfactory fit for **1** was obtained with $J = -7.0$ cm^{-1}, $g = 1.95$, $D = -8$ cm^{-1} (assumed to be the same for dimers and monomers), and $f = 0.24$. The best fit of the experimental data for **2** is achieved with the following parameters: $J = -1.10$ cm^{-1}, $g = 1.95$, $D = -8$ cm^{-1} for dimers and $D = -16$ cm^{-1} for monomers, and $f = 0.30$. Figures S13 and S14 in the SI collect the temperature dependence of the magnetic data for **2**. The discrepancy between the magnetic susceptibilities for these complexes would arise from the presence of different amounts of mononuclear paramagnetic manganese(III), and J values for **1** and **2** should be taken with caution.

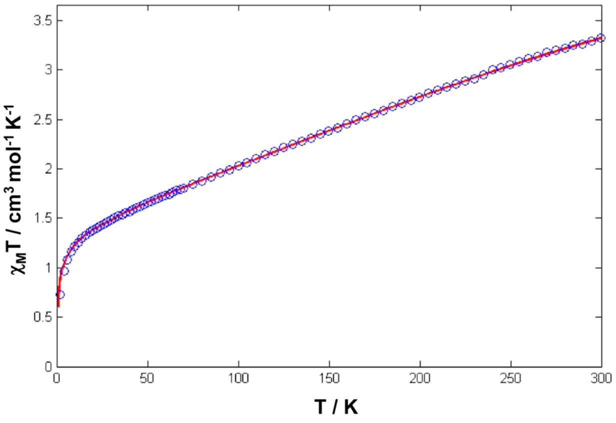

Figure 7. Temperature dependence of $\chi_M T$ on T for **1**. The blue circles correspond to observed data and the red line to the best data fit, with χ_M being the molar magnetic susceptibility.

Catalytic Studies. The ability to vary the size of the cavities in these new redox-active materials may provide access to tunable frameworks that can be matched with the desired application. We believe that the approach reported herein could open new perspectives for the design of selective catalysts in different redox processes.

These supramolecular boxes incorporate the redox-active manganese(III) ion, and they could be used as catalysts for different processes. For example, catalase-like activity could be one of the most interesting applications. Manganese catalases are able to disproportionate H_2O_2 into H_2O and O_2. These enzymes protect organisms against oxidative stress by removing appreciable levels of H_2O_2, which is a byproduct of respiration.[38]

Excessive concentrations of reactive oxygen species can have serious adverse effects on living systems, including peroxidation of membrane lipids, hydroxylation of nucleic acid bases, and oxidation of sulfhydryl groups and other sensitive moieties in proteins.[39] If uncontrolled, mutations and cellular death result.[40,41] Owing to their potencial application as therapeutic agents against oxidative stress, various biomimetic mononuclear manganese complexes have been selected for pharmaceutical uses as $O_2^{\bullet-}$ scavengers,[42] and a number of dinuclear manganese-based complexes has been investigated as low-molecular-weight catalytic scavengers of H_2O_2.[43]

We evaluated the disproportionation of H_2O_2 catalyzed by **1**–**3** by volumetric determination of the evolved O_2. The good solubility of these supramolecular boxes in different solvents facilitates these experiments in biological media. The experimental setup was evaluated by the measurements for the catalytic decomposition of H_2O_2 (2.5×10^{-3} mol) with MnO_2: ca. 30 mL of O_2 evolution was measured by a buret, which agrees with the calculated value based on the assumption that catalytic decomposition of H_2O_2 to H_2O and O_2 takes place.

Table 5 collects the results of the catalase activities. All three complexes showed significant rates of catalase activity, with 100% H_2O_2 decomposition achieved in 20 min at 36 °C upon using compound **1** with a peroxide/catalyst ratio of 667. Complex **1** appears to be stable over 1200 catalytic turnovers. The time course of oxygen production is similar for each of the complexes. The reaction proceeds quickly during the first 5−10 min, and over time, the total amount of oxygen evolved approaches an asymptotic limit.

Table 5. Catalytic Activity for 1−3 in the Catalase-like Function, Peroxidase Action, and Capacity of Oxidation of VA

		catalase activity (in MeOH)			
complex		23 °C	36 °C	peroxidase activity	oxidation of VA[a]
1	turnovers[b]	667 ± 1	667 ± 1		
	% activity	100 ± 2	100 ± 2	2 ± 0.5	nob
2	turnovers	162 ± 6	368 ± 22		
	% activity	25 ± 3	55 ± 7	1 ± 0.3	nob
3	turnovers	110 ± 5	384 ± 8		
	% activity	17 ± 3	58 ± 4	1 ± 0.5	nob

[a] nob = not observable. [b] Turnover numbers after 60 min, except for the catalase activity of **1**, which catalyzes the decomposition of 100% H_2O_2 at 36 °C in 20 min in the cited experimental conditions.

Complexes **1**−**3** also show catalytic activity in H_2O oxidation and subsequent O_2 production under light irradiation and in the presence of a hydrogen acceptor (BQ). The molecule of H_2O is a small substrate that is able to enter into the cavity of the supramolecular box. Light absorption at 425 nm in an aqueous solution causes a $\pi^* \leftarrow n$ transition, and this is responsible for hydrogen abstraction from H_2O by optically excited BQ (BQ*).[44] The course of the water photolysis experiments was followed in two ways: quantitative oxygen evolution and variation of the electronic spectrum of quinone during photolysis.[24] The concentration of O_2 in the solutions during the experiments increased from about 3% dissolved oxygen, to 13.1% for photolysis catalyzed by complex **1**, to 10% for photolysis catalyzed by complex **2**, and to 10.2% for photolysis catalyzed by complex **3**. The reduction of BQ to hydroquinone (H_2BQ) can be easily followed by UV spectroscopy (Figure 8). BQ in H_2O has a major absorption at 246 nm ($\varepsilon = 2.2 \times 10^4$ M^{-1} cm^{-1}), which decreased during the experiments, while a characteristic H_2BQ peak at 290 nm developed. The time courses of the absorbances at 246 and 290 nm are collected in Figures S15 and S16 in the SI.

Additional studies highlighted how the supramolecular box structure of these compounds increases the selectivity of the catalytic processes. Thus, we demonstrated the lack of activity of these complexes in peroxidase action upon using bulky organic substrates such as ABTS [the diammonium salt of 2,2′-azinobis(3-ethylbenzothiazoline-6-sulfonic acid)], guaiacol, or the lignin analogue VA.

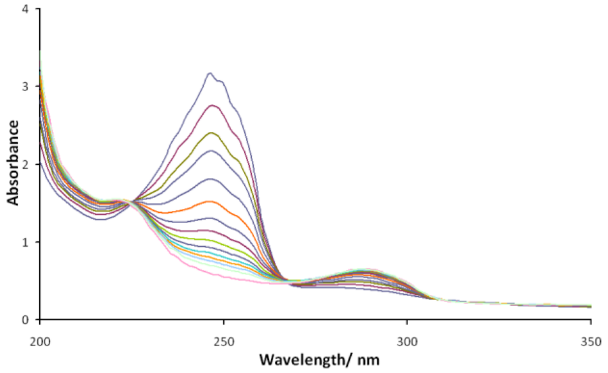

Figure 8. Evolution of the UV spectra during the water photolysis experiments for **1**, showing a decrease of the 246 nm band (disappearance of BQ) and an increase of the 290 nm band (formation of H_2BQ).

ABTS is colorless, and it reacts readily with H_2O_2 in the presence of a peroxidase catalyst to yield a stable green radical cation $ABTS^{\bullet+}$,[45] which presents characteristic absorption bands at 415, 650, 735, and 815 nm (Figure S17 in the SI). The extent of the reaction can be measured quantitatively at λ = 650 nm because ε = 12000 M^{-1} cm^{-1} has been determined. The oxidation potential of ABTS to provide $ABTS^{\bullet+}$ is invariable over a wide range of pH values. In the absence of the complex, a solution of ABTS and H_2O_2 is stable for several hours without showing any formation of $ABTS^{\bullet+}$. Complexes **1**−**3** do not show significant peroxidase-like activity because the UV absorbances corresponding to the $ABTS^{\bullet+}$ radical cation are negligible in the assays with these complexes.

Oxidation of guaiacol (2-methoxyphenol) by manganese peroxidases in the presence of H_2O_2 produces tetraguaiacol. This process can be monitored by absorbance at 470 nm.[46] Complexes **1**−**3** show a significant rate of guaiacol oxidation because their UV−vis spectra is hardly altered during the guaiacol oxidation assay. In contrast, monomeric manganese complexes show relevant peroxidase activity. Figures S18 and S19 in the Supporting Information compare the results of this oxidation assay with **1**−**3** and with a monomeric $[MnL(H_2O)(OAc)](H_2O)$ complex (where L = *N*,*N*′-bis(3-OMe-salicylidene)-1,2-diphenylenediamine), previously reported by us.[14] An increase in the tetraguaicol absorbance at 470 nm is clearly observed by catalysis with this monomeric system but not with complexes **1**−**3**.

The peroxidase activity using the bulky ABTS substrate of the same monomeric $[MnL(H_2O)(OAc)](H_2O)$ complex and employing an analogous experimental procedure gives a conversion rate of about 33%, 30-fold higher than that for the activity measured for **1**−**3**. Nevertheless, the catalase activity reported for this monomeric manganese complex is lower than that for **1**−**3**. A comparison of the catalytic behavior of compounds **1**−**3** and monomeric complexes reinforces the selectivity of the catalytic processes driven by the supramolecular boxes.

VA is a commonly used lignin model.[47] Oxidative degradation of VA by manganese peroxidases yields veratraldehyde, which absorbs strongly at 310 nm (ε = 9300 M^{-1} cm^{-1}).[48] This reaction may then be followed by UV spectroscopy through variation of the absorbance at this wavelength. We have also purified the resulting mixture by column chromatography using a procedure already reported by us.[49] The main product was characterized by NMR spectroscopy and identified as VA [^{1}H NMR (300 MHz): δ 7.02 (s, 1H), 6.79 (d, 1H), 6.53 (d, 1H), 4.61 (s, 2H), 3.83 (s, 6H)]. Veratraldehyde was not detected by UV or NMR spectroscopy.

Complexes **1**−**3** do not show catecholase activity using 3,5-$DTBCH_2$ as a different bulky substrate. The catecholase activity is the catalytic process of oxidation of *o*-diphenolcatechol to 3,5-DTBQ coupled with $2e^-/2H^+$ reduction of O_2 to H_2O.[50] Regarding manganese compounds, some mononuclear, dinuclear, and oligonuclear systems are known to act as catalysts for catecholase activity.[51] In order to contrast this activity, we have also carried out the catecholase experiments using a di-μ-oxomanganese dimer, $[Mn(3,5\text{-}Brsalpn)O]_2$, previously reported by us.[52] UV−vis spectra of complexes **1**−**3** and $[Mn(3,5\text{-}Brsalpn)O]_2$ in the presence of 3,5-$DTBCH_2$ are shown in Figure S20 in the SI. A band with a maximum in the region 380−390 nm, corresponding to the formation of 3,5-DTBQ, is only generated using $[Mn(3,5\text{-}Brsalpn)O]_2$ as the catalyst. The plot of variation of the absorbance at 380 nm versus time for **1**−**3** in the presence of 3,5-$DTBCH_2$ (Figure S21 in the SI) clearly shows the lack of catecholase activity for these complexes.

The square-pyramidal geometry of the manganese ion in complexes **1**−**3** is optimal for catalytic activity because the potential catalyst has a vacancy in the coordination sphere where the substrate molecule may be located. Our findings show that these compounds behave as active catalysts for water photolysis and for disproportionation of H_2O_2, but they do not catalyze peroxidase action upon using bulky organic substrates such as ABTS, guaiacol, or VA. Catecholase activity is not found for these supramolecular boxes. A detailed kinetic study of this catalytic process merits further investigation in order to propose the reaction mechanism for these catalase mimics and also to determine whether the fact that the bulky substrates are unable to enter into the cavity of the supramolecular box is the key factor in their catalytic performance.

■ CONCLUSION

We have prepared three supramolecular boxes from manganese(III) complexes and have successfully established a new synthetic route that involves self-assembly induced by alkali-metal ions. These compounds can act as selective catalysts in different redox processes in cases where the substrate molecule is able to enter into the cavity of the box.

We have assessed the catalase activity of these systems in decomposition of the H_2O_2 molecule. The size of the cavity of the supramolecular box can be tuned depending on the alkali metal used, a characteristic that gives this new family of catalysts the potential to act selectively against different substrates.

■ ASSOCIATED CONTENT

Ⓢ Supporting Information

X-ray crystallographic data in CIF format, selected bond distances and angles for H_4L, $^1H/^{13}C$ NMR spectra for H_4L, molecular packing for H_4L, IR spectrum for H_4L and **3**, ESI-MS for H_4L and **3**, paramagnetic NMR for **3**, plots of magnetic data versus temperature for **1**−**3**, plots of variation of the 246 and 290 nm absorbance during photolytic experiments, reaction of oxidation of ABTS in $ABTS^{\bullet+}$, UV−vis spectra, variation of the absorbance for guaiacol oxidation assays, and catecholase activity experiments. This material is available free of charge via the Internet at http://pubs.acs.org.

■ AUTHOR INFORMATION

Corresponding Authors

*E-mail: misabel.fernandez.garcia@usc.es.
*E-mail: marcelino.maneiro@usc.es.

Present Address

§M.J.R.-D.: Dipartamento di Farmacia, Universitá degli Studi di Pisa, 56126 Pisa, Italy.

Notes

The authors declare no competing financial interest.

■ ACKNOWLEDGMENTS

Financial support from the Spanish Ministerio de Ciencia e Innovación (Grant CTQ2010-19191) and Xunta de Galicia (Grant 10PXIB262132PR) is acknowledged.

■ REFERENCES

(1) Constable, E. C. In *Comprehensive Supramolecular Chemistry*; Sauvage, J. P., Hosseini, M. W., Eds.; Pergamon Press: Oxford, U.K., 1996; Vol. *9*, p 213.

(2) Albrecht, M. *Chem. Rev.* **2001**, *101*, 3457−3498.

(3) (a) Moriwaka, M.; Kimizuka, N. *Chem. Commun.* **2012**, *48*, 11106. (b) Lee, S. J.; Cho, S.-H.; Mulfort, K. L.; Tiede, D. M.; Hupp, J. T.; Nguyen, S. T. *J. Am. Chem. Soc.* **2008**, *130*, 16828−16829. (c) Indelli, M. T.; Chiorboli, C.; Scandola, F.; Iengo, E.; Osswald, P.; Würthner, F. *J. Phys. Chem. B* **2010**, *114*, 14495−14504.

(4) Jurícek, M.; Barnes, J. C.; Dale, E. J.; Liu, W.-G.; Strutt, N. L.; Bruns, C. J.; Vermeulen, N. A.; Ghooray, K. C.; Sarjeant, A. A.; Stern, C. L.; Botros, Y. Y.; Goddard, W. A.; Stoddart, J. F. *J. Am. Chem. Soc.* **2013**, *135*, 12736−12746.

(5) (a) Kleij, A. W.; Kuil, M.; Tooke, D. M.; Lutz, M.; Spek, A. L.; Reek, J. N. H. *Chem.—Eur. J.* **2005**, *11*, 4743−4750. (b) Albrecht, M.; Isaak, E.; Baumert, M.; Gossen, V.; Raabe, G.; Froehlich, R. *Angew. Chem.* **2011**, *123*, 2903−2906. (c) Bolliger, J. L.; Belenguer, A. M.; Nitschke, J. R. *Angew. Chem., Int. Ed.* **2013**, *52*, 7958−7962. (d) Han, M.; Michel, R.; He, B.; Chen, Y.-S.; Stalke, D.; John, M.; Clever, G. H. *Angew. Chem., Int. Ed.* **2013**, *52*, 1319−1323.

(6) Hannon, M. J.; Painting, C. L.; Errington, W. *Chem. Commun.* **1997**, 307−308.

(7) Bermejo, M. R.; González-Noya, A. M.; Pedrido, R.; Romero, M. J.; Vázquez, M. *Angew. Chem., Int. Ed.* **2005**, *44*, 4182−4187.

(8) (a) M. Lutz, M.; Haukka, M.; Pakkanen, T. A.; Gade, L. H. *Inorg. Chem.* **2003**, *42*, 2798−2804. (b) Chen, G.-J.; Gao, F.-X.; Huang, F.-P.; Tian, J.-L.; Gu, W.; Liu, X.; Yan, S.-P.; Liao, D.-Z. *Cryst. Growth Des.* **2009**, *9*, 2662−2667. (c) Pradeep, C. P.; Long, D.-L.; Cronin, L. *Dalton Trans.* **2010**, *39*, 9443.

(9) Marin, K. E.; Wang, Z.; Busani, T.; Garcia, R. M.; Chen, Z.; Jiang, Y.; Song, Y.; Jacobsen, J. L.; Vu, T. T.; Schore, N. E.; Swartzentruber, B. S.; Medforth, C. J.; Shelnutt, J. A. *J. Am. Chem. Soc.* **2010**, *132*, 8194−8201.

(10) Ruhlandt-Senge, K.; Torvisco, A. *Inorg. Chem.* **2011**, *50*, 12223−12240.

(11) Faul, C. F. J.; Antonietti, M. *Adv. Mater.* **2003**, *15*, 673−683.

(12) Torvisco, A.; Decker, K.; Uhlig, F.; Ruhlandt-Senge, K. *Inorg. Chem.* **2009**, *48*, 11459−11465.

(13) Lorena-Cortez, M.; Pallarola, D.; Ceolín, M.; Azzaroni, O.; Battaglini, F. *Chem. Commun.* **2012**, *48*, 10868−10870.

(14) Vázquez-Fernández, A.; Bermejo, M. R.; Fernández-García, M. I.; González-Riopedre, G.; Rodríguez-Doutón, M. J.; Maneiro, M. *J. Inorg. Biochem.* **2011**, *105*, 1538−1547.

(15) Costes, J.-P.; Dahan, F.; Donnadieu, B.; Rodríguez-Douton, M. J.; Fernández-Garcia, M. I.; Bousseksou, A.; Tuchages, J.-P. *Inorg. Chem.* **2004**, *43*, 2736−2744.

(16) Sheldrick, G. M. *SHELX-97 (Shelxs 97 and Shelxl 97), Programs for Crystal Structure Analyses*; University of Göttingen: Göttingen, Germany, 1998.

(17) Sheldrick, G. M. *SADABS, Program for Scaling and Correction of Area Detector Data*; University of Göttingen: Göttingen, Germany, 1996.

(18) Sheldrick, G. M. *Acta Crystallogr.* **2008**, *A64*, 112−122.

(19) Macrae, C. F.; Bruno, I. J.; Chisholm, J. A.; Edgington, P. R.; McCabe, P.; Pidcock, E.; Rodriguez-Monge, L.; Taylor, R.; van de Streek, J.; Wood, P. A. *J. Appl. Crystallogr.* **2008**, *41*, 466−470.

(20) Geary, W. J. *Coord. Chem. Rev.* **1971**, *7*, 81−122.

(21) Daier, V.; Moreno, D.; Duhayon, C.; Tuchagues, J.; Signorella, S. *Eur. J. Inorg. Chem.* **2010**, 965−974.

(22) Collomb, M.-N.; Mantel, C.; Romain, S.; Duboc, C.; Leprêtre, J.-C.; Pécaut, J.; Deronzier, A. *Eur. J. Inorg. Chem.* **2007**, 3179−3187.

(23) Bonadies, J. A.; Maroney, M. L.; Pecoraro, V. L. *Inorg. Chem.* **1989**, *28*, 2044−2051.

(24) González-Riopedre, G.; Fernández-García, M. I.; González-Noya, A. M.; Vázquez-Fernández, M. A.; Bermejo, M. R.; Maneiro, M. *Phys. Chem. Chem. Phys.* **2011**, *13*, 18069−18077.

(25) Adarsh, N. N.; Kumar, D. K.; Dastidar, P. *CrystEngComm* **2009**, *11*, 796−802.

(26) Fun, H.-K.; Chinnakali, K.; Razak, I. A.; Shen, Z.; Zuo, J.-L.; You, X.-Z. *Acta Crystallogr.* **1999**, *C55*, 99−100.

(27) Leung, W.-H.; Hun, T. S. M.; Hui, K.-N.; Williams, I. D. *Polyhedron* **1996**, *3*, 421−426.

(28) Jensen, K. B.; Johansen, E.; Larsen, F. B.; McKenzie, C. J. *Inorg. Chem.* **2004**, *43*, 3801−3803.

(29) Murray, C.; Gildea, B.; Müller-Bunz, H.; Harding, C. H.; Morgan, G. G. *Dalton Trans.* **2012**, *41*, 14487−14489.

(30) Bermejo, M. R.; Fernández, M. I.; González-Noya, A. M.; Maneiro, M.; Pedrido, R.; Rodríguez, M. J.; García-Monteagudo, J. C.; Donnadieu, B. *J. Inorg. Biochem.* **2006**, *100*, 1470−1478.

(31) Zuniga, M. F.; Deacon, G. B.; Ruhlandt-Senge, K. *Inorg. Chem.* **2008**, *47*, 4669−4681.

(32) Berben, L. A.; Long, J. R. *J. Am. Chem. Soc.* **2002**, *124*, 11588−11589.

(33) Pascal, P. *Ann. Chim. Phys.* **1910**, *19*, 5−70.

(34) O'Connor, C. J. *Prog. Inorg. Chem.* **1982**, *29*, 203−283.

(35) Garge, P.; Chikate, R.; Padhye, S.; Savariault, J. M.; De Loth, P.; Tuchagues, J.-P. *Inorg. Chem.* **1990**, *29*, 3315−3320.

(36) Stoicescu, L.; Duhayon, C.; Vendier, L.; Tesouro-Vallina, A.; Costes, J.-P.; Tuchagues, J.-P. *Eur. J. Inorg. Chem.* **2009**, 5483−5493.

(37) (a) Matsumoto, N.; Zhang, Z. J.; Okawa, H.; Kida, S. *Inorg. Chim. Acta* **1989**, *160*, 153−163. (b) Miyasaka, H.; Clérac, R.; Ishii, T.; Chang, H.-C.; Kitagawa, S.; Yamashita, M. *J. Chem. Soc., Dalton Trans.* **2002**, 1528−1534.

(38) Calabrese, V.; Cornelius, C.; Mancuso, C.; Pennisi, G.; Calafato, S.; Bellia, F.; Bates, T. E.; Giuffrida-Stella, A. M.; Schapira, T.; Dinkova-Kostova, A. T.; Rizzarelli, E. *Neurochem. Res.* **2008**, 33, 2444−2471.

(39) Watt, R. K. *ChemBioChem* **2013**, *14*, 415−419.

(40) Alireza, R.; Razieh, Y. *Clin. Biochem.* **2011**, *44*, S227−S228.

(41) Snell, T. W.; Fields, A. M.; Johnston, R. K. *Biogerontology* **2012**, *13*, 261−275.

(42) (a) Doctrow, S. R.; Liesa, M.; Melov, S.; Shirihai, O. S.; Tofilon, P. *Curr. Inorg. Chem.* **2012**, *2*, 325−334. (b) Batinic-Haberle, I.; Reboucas, J. S.; Spasojevic, I. *Antioxid. Redox Signaling* **2010**, *13*, 877−918. (c) Dismukes, G. C.; Brimblecombe, R.; Felton, G. A. N.; Pryadun, R. S.; Sheats, J. E.; Spiccia, L.; Swiegers, G. W. *Acc. Chem. Res.* **2009**, *42*, 1935−1943. (d) Day, B. J. *Biochem. Pharmacol.* **2009**, *77*, 285−296.

(43) (a) Bani, D.; Bencini, A. *Curr. Med. Chem.* **2012**, *19*, 4431−4444. (b) Signorella, S.; Hureau, C. *Coord. Chem. Rev.* **2012**, *256*, 1229−1245. (c) Bhabak, K. P.; Mugesh, G. *Acc. Chem. Res.* **2010**, *43*, 1408−1419. (d) Lessa, J. A.; Horn, A., Jr.; Bull, E. S.; Rocha, M. R.; Benassi, M.; Catharino, R. R.; Eberlin, M. N.; Casellato, A.; Noble, C. J.; Hanson, G. R.; Schenk, G.; Silva, G. C.; Antunes, O. A. C.; Fernandes, C. *Inorg. Chem.* **2009**, *48*, 4569−4579. (e) Boelrijk, A. E. M.; Dismukes, G. C. *Inorg. Chem.* **2000**, *39*, 3020−3028.

(44) Awad, M.; Anderson, A. *J. Am. Chem. Soc.* **1989**, *111*, 802−806.

(45) Eulering, B.; Schmidt, M.; Pinkernell, V.; Karst, U.; Krebs, B. *Angew. Chem., Int. Ed.* **1996**, *35*, 1973−1974.

(46) Hayashi, T.; Murata, D.; Makino, M.; Sugimoto, H.; Matsuo, T.; Sato, H.; Shiro, Y.; Hisaeda, Y. *Inorg. Chem.* **2006**, *45*, 10530−10536.

(47) Kervinen, K.; Lahtinen, P.; Repo, T.; Svanh, M.; Leskela, M. *Catal. Today* **2002**, *75*, 183−188.

(48) Liu, A.; Huang, X.; Song, S.; Wang, D.; Xuemei, L.; Qu, Y.; Gao, P. *Spectrochim. Acta, Part A* **2003**, *59*, 2547−2551.

(49) González-Riopedre, G.; Fernández-García, M. I.; Gómez-Fórneas, E.; Maneiro, M. *Catalysts* **2013**, *3*, 232−246.

(50) Koval, I. A.; Gamez, P.; Belle, C.; Selmeczi, K.; Reedijk, J. *Chem. Soc. Rev.* **2006**, *35*, 814.

(51) Jana, A.; Aliaga-Alcalde, N.; Ruiz, E.; Mohanta, S. *Inorg. Chem.* **2013**, *52*, 7732−7746.

(52) Maneiro, M.; Bermejo, M. R.; Fondo, M.; González, A. M.; Sanmartín, J.; García-Monteagudo, J. C.; Pritchard, R. G.; Tyryshkin, A. M. *Polyhedron* **2001**, *20*, 711−719.